Noncontact Measurement of Breathing Function

BY RAMYA MURTHY
AND IOANNIS PAVLIDIS

A Novel Method Using Infrared Imaging and Advanced Statistics

We have developed a novel method for noncontact measurement of breathing function. The method is based on the statistical modeling of dynamic thermal data captured through a highly sensitive infrared imaging system. The air that is breathed out has a higher temperature than the typical background of indoor environments (e.g., walls). Therefore, the particles of the expired air emit at a higher power than the background, a phenomenon that is captured as a distinct thermal signature in the infrared imagery. There is significant technical difficulty in computing this signature, however, because the phenomenona has a very low intensity and is of a transient nature. To address the problem, we use an advanced statistical algorithm based on multinormal data representation, the method of moments, and the Jeffreys divergence measure. In experimental tests, we were able to correctly compute the breathing waveforms in eight infrared video clips of three subjects at distances ranging 6–8 ft. The results were compared with ground-truth data collected concomitantly with a traditional contact sensor. Our experiments demonstrated the promise of this modality, which may find applications in the next generation of contact-free polygraphy and in sleep studies.

Monitoring of breathing function has applications in polygraphy, sleep studies, sport training, early detection of sudden infant death syndrome in neonates, and patient monitoring.

Various contact measurement methods have been developed for estimating the breathing rate of a subject. Moody et al. developed a contact modality in which numerous electrocardiogram (ECG) electrodes and sensors are attached to the subject [1]. The principle of operation is based on the fact that the heart rate is typically modulated by breathing, a phenomenon known as sinus arrhythmia [2]. Therefore, a signal corresponding to the heart function contains breath information, which is filtered out using band-pass filters.

As an improvement over the ECG method, the BioMatt method [3] was developed in Finland by a group of researchers who were studying sleep disorders. BioMatt performs measurements of vital signs, such as breathing and cardiac activity without electrodes. Initially, BioMatt could not distinguish motion that was due to breathing versus cardiac activity or body movement. Later, Larson developed a signal processing technique to separate out the components of the BioMatt signal [4].

Photoplethysmography (PPG) is a variant method of the ECG, developed to measure blood volume changes in living tissues by absorption or scattering of

0739-5175/06/$20.00©2006IEEE

near-infrared radiation. This modality consists of an infrared light-emitting diode (LED) and a photodiode that can be clamped to the ear lobes, thumbs, or toes. It is advantageous because it is portable, compact, and needs very little maintenance. The measurement of blood volume changes by PPG depends on stronger absorption of near-infrared light by blood when compared to other superficial tissues [5]. The amount of backscattered light corresponds to the variation of the blood volume. As in ECG, the breath waveform is separated from the cardiac signal through various methods that have been developed [6], [7]. However, using heart function as a basis for acquiring the breathing waveform is unreliable since sinus arrhythmia is not present in all individuals. Control of cardiac activity by breathing depends on the age and medications administered to subjects.

Other contact modalities are capable of directly measuring the breathing signal. An example of such modality is the abdominal strain gauge transducer [8], which is strapped around the subject's chest and measures the change in thoracic or abdominal circumference while breathing. Another example is a thermistor that measures nasal air temperature variation as an indication of breathing [9].

The disadvantage of all the aforementioned technologies is that they require close contact with the subject, which, in certain cases, may be quite uncomfortable and awkward (e.g., abdominal transducer). A contact-free but active technology called *radar vital signs monitor* (RVSM) [10] was developed in 1996 to monitor the performance of Olympic athletes. The RVSM detects breathing-induced movement of the chest based on the Doppler phenomenon. It measures breath at distances of up to 15 ft behind an 8-in hollow concrete or wooden wall. A radar flashlight [11] was built to make use of this capability in assisting law enforcement personnel to detect individuals hidden behind walls. In 2000, RVSM was used in noncontact polygraphy [12]. The disadvantage of this technique is that motion artifacts corrupt breath signals, and specialized frequency filters need to be used to separate them.

In 2000, infrared imaging proved its potential in deception detection when thermal image analysis was used by Pavlidis et al. to detect facial patterns of stress at a distance [13]. A little later, Pavlidis et al. used infrared imaging to compute periorbital perfusion as a replacement of the corresponding polygraph channel that uses finger contact sensing [14], [15]. The proposed use of infrared imaging for computing breathing function may also replace the corresponding polygraph channel that uses the abdominal transducer. Incremental replacement of contact channels with noncontact ones may prove very effective in the field of polygraphy, where it is essential that subjects feel as comfortable as possible during examination.

Moreover, highly automated, noncontact monitoring of breathing function may have a significant impact on certain biomedical applications. For example, in sleep studies, this new methodology will enable monitoring of sleep apnea with minimal or no wiring of the subject, potentially at his/her home and not in the lab. This will not only improve the subject's comfort but also facilitate much more sustained monitoring than is currently feasible.

The use of infrared imaging for measuring breathing function is based on the fact that the exhaled air has a higher temperature than the typical background of indoor environments. This creates a discriminating thermal signature that can be captured through an infrared imaging sensor. The phenomenon is quasiperiodic and can be quantified using either statistics or calculus. From the statistical point of view, one can model the breathing cycles as multinormal distributions—one with cold temperatures corresponding to inhalation and one with hot temperatures corresponding to exhalation. From the Calculus point of view, one can model the quasiperiodicity of breathing through Fourier analysis.

In this article, we describe a statistically based methodology for quantifying breathing rate with infrared imaging data. Alternative methodologies, like Fourier analysis, can be used but are not addressed in our present work. Our goal is to open a new line of research by demonstrating the feasibility of monitoring breathing function in a highly automated and noncontact fashion.

In this article, we describe briefly the physiology of breathing. Then we refer to the visual tracking mechanism that enables consistent breathing measurements in the presence of subject motion. Our breath visualization scheme, which is of paramount importance during the training phase of our measurement algorithm, is described, and we explain in great detail the statistical algorithm that performs the breathing measurement on the infrared imaging data. Next, we outline our experimental design and results, and we finally conclude by discussing the strong and weak points of our methodology, its prospects, and our planned work for the future.

Breathing Function

Respiration in a man involves three well-defined stages [16]. The first stage is breathing. It comprises inspiration, taking oxygenated air into the lungs, and expiration, discharging air that is rich in carbon dioxide. The second stage involves the transport of the oxygen to the cells of the body using the heart and the vascular system. The third stage is called *cellular respiration*; in this stage, oxygen is used in the process of generating energy for physiological activities.

In our study, we are interested in monitoring breathing using infrared imaging. The breathing cycle consists of inspiration, expiration, and postexpiratory pause. During quiet breathing, inspiration begins due to negative pressure

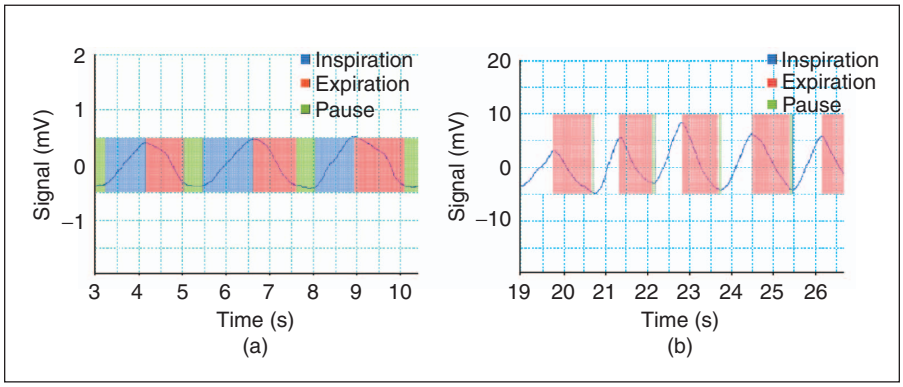

Fig. 1. Output from a piezo-respiratory belt transducer showing the three breathing phases during (a) quiet breathing and (b) after exercise.

created inside the chest cavity by the contraction of the diaphragm. Expiration is a passive process where the air flow occurs due to the elastic recoil property of the lungs. The postexpiratory pause is caused when there is equalization of the pressures inside the lungs and the atmosphere.

Breathing cycle is defined as the time interval between the beginning of inspiration and the end of postexpiratory pause. During quiet breathing, the breathing rate may vary from 12–20 breaths/min and, after physical activity, 30–40 breaths/min in healthy individuals. Figure 1(a) and (b) shows typical duration of the three phases during quiet breathing and after physical activity, respectively.

During quiet breathing, the duration of postexpiratory pause is comparable to that of inspiration and expiration. After a person undergoes physical exertion, the postexpiratory duration reduces considerably and, in some cases, this phase may even cease to exist.

Tracking the Region of Interest

We define as the region of interest (ROI) R the region in the background, where there is possible presence of respiratory airflow. It is in this small image region that our statistical algorithm is applied. The ROI is characterized by its size, shape, and position. Over time, the size and shape of ROI remain the same, but its position changes to cope with the subject's motion (tracking). We have experimented with different ROI sizes, and we will give more details about the optimal determination of this parameter later. In this section, we will address the issues of ROI shape and dynamic positioning.

For simplicity, R was chosen to be a rectangular region. Typically, subjects are breathing through the nasal cavity, which results in a downward airflow profile. Breathing through the mouth is less prevalent and results in horizontal airflow profile. In our dataset, we observed downward airflow profiles [Figure 2(a)] in seven video clips and a horizontal profile [Figure 2(b)] in one video clip. Hence, we chose a rectangular region R arranged in a longitudinal fashion to closely match the prevalent downward profile of airflow. Our experiments have also shown that this shape still worked quite well on the video clip featuring the horizontal airflow profile (97.74% accuracy).

The respective aims of the initial positioning and tracking algorithms are to provide the user with an approximate position of the ROI in the vicinity of the nasal-mandible region and follow it automatically throughout the breathing rate computation process. Technical details of the initial positioning and tracking algorithms can be found in [17]. The initial positioning algorithm locates the tip of the subject's nose and places the ROI underneath it, in a position that is between the nostrils and the mouth (Figure 3). This placement works for the typical monitoring scenario of a subject imaged at a side view. For different monitoring scenarios, the above heuristic approach tends to place R incorrectly. But, the graphical user interface (GUI) gives options to move the ROI around the image so it can be placed within the airflow with just a mouse click. In such adjustments, the user is aided by the breath visualization tool. Hence, the initial positioning of ROI is semiautomatic; the algorithm gives the approximate position of R, and then the user may need to move it to a better position within the field of the airflow. By contrast, the tracking algorithm is completely automatic since it tracks R with respect to the tip of the nose in subsequent video frames without any feedback from the user.

Visualization of Breath

Visualization is important for, among other reasons, adjusting the initial ROI position and for training the statistical algorithm. Since the thermal signature of breath is not very strong, we have to apply image processing techniques to visually perceive breath in infrared video frames. Specifically, we apply the following operations on the video clip frames:

1) Otsu's adaptive thresholding [18]
2) differential infrared thermography (DIT) [19]
3) image opening [20].

Otsu's adaptive thresholding is applied to segment the skin region from the background. Then, in the background region, we apply DIT to generate a breath mask of all pixels whose temperature has increased beyond a preset threshold. This operation makes sure that the colormap is applied only to expiration frames in which DIT senses an increase in ROI pixel temperatures above the preset value. The result is a highly contrasting effect of no color during inspiration versus vivid color during expiration [see Figure 3(a) and (b)]. As a final step, an image open operation is applied on the output binary mask of DIT to improve breath visualization.

The visualization scheme works well only for a limited period, as the temperature distributions of inspiration and expiration tend to drift over time for physiological and other reasons. DIT cannot handle this distribution drift well. If it did, it could have also been used to measure breathing rate in the place of the more sophisticated statistical algorithm (see the following section). However, the short time window of good visualization performance is adequate for adjusting the initial ROI position and training the statistical algorithm.

Statistical Methodology

Integral to breathing rate computation using infrared imaging is the labeling of frames as expiratory and

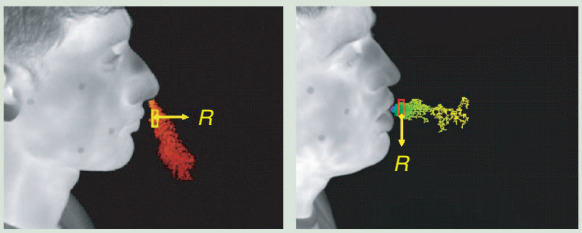

Fig. 2. Respiratory airflow profiles: (a) downward and (b) horizontal.

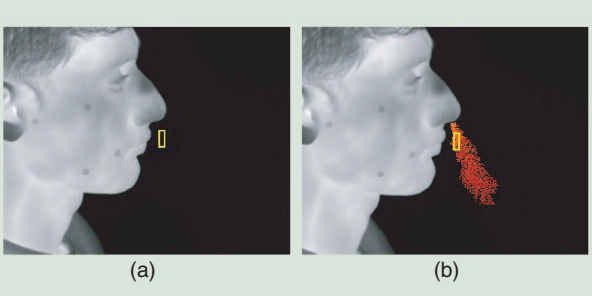

Fig. 3. Visualization of breath during (a) nonexpiration and (b) expiration. The ROI is anchored just under the subject's nose tip.

Monitoring of breathing function has applications in polygraphy, sleep studies, sport training, and patient monitoring.

nonexpiratory. For this purpose, we have adopted a statistical methodology based on multinormal distributions, the method of moments, and the Jeffreys divergence measure [21]. We identify two phases in the statistical method: training and testing. We describe both phases in subsequent sections.

First, we ascertain the normal nature of the temperature distributions in the ROI for the various breathing stages (Figure 4). Therefore, we can represent ROI distributions by their mean μ and variance σ^2 only. Our method combines inspiration and postexpiratory pause phases, since the thermal signatures of these two are almost identical. We designate the combined stage as nonexpiratory phase.

Training Phase

The algorithm runs through a training phase to generate estimates of the expiration and nonexpiration distributions from the first few video frames. These estimates are then used to label pixels as expiratory or nonexpiratory in the initial video frame of the testing phase.

We use a variant of the *K*-means clustering algorithm [22] to generate training data. Our objective is to form $K = 2$ representative distributions through an iterative process; a hot one for expiration and a cold one for nonexpiration. Initially, we specify as the expiration distribution $D_{e,0}$ the one with the hottest mean temperature $\mu_{e,0}$ in the training set; we specify as the nonexpiration distribution $D_{i,0}$ the one with the coldest mean temperature $\mu_{i,0}$ in the training set:

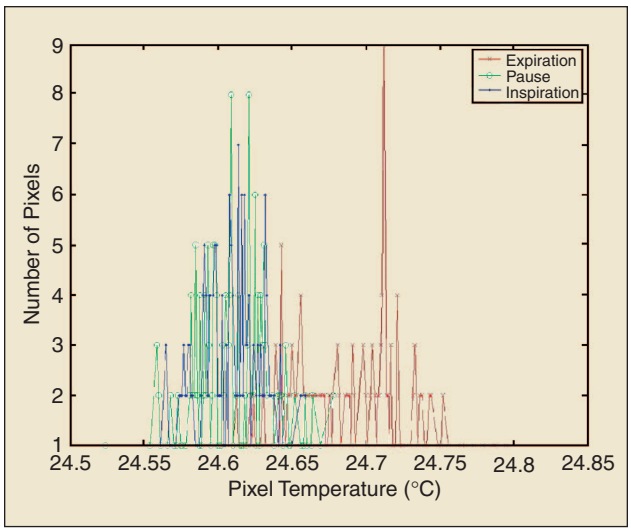

Fig. 4. Experimental temperature distributions for expiration, postexpiratory pause, and inspiration. The normal nature of the distributions and overlapping between postexpiratory pause and inspiration are evident.

$$\mu_{e,0} = \max_{1 \le j \le M} \{\mu_j\}, \tag{1}$$

$$\mu_{i,0} = \min_{1 \le j \le M} \{\mu_j\}, \tag{2}$$

where $N(\mu_j, \sigma_j^2)$, $1 \le j \le M$ is the set of temperature distributions for ROI R corresponding to the first $M = 100$ training frames of infrared video. We sort the distributions in ascending order with respect to their means in order to facilitate the iterative process.

On every step j, $1 \le j \le M$, we find the statistical distance of distribution $D_j \sim N(\mu_j, \sigma_j^2)$ from $D_{e,j-1}$ and $D_{i,j-1}$. For this purpose, we use the Jeffreys divergence measure as follows:

$$J(D_{e,j-1}D_j) = \frac{1}{2}\left(\frac{\sigma_{e,j-1}}{\sigma_j} - \frac{\sigma_j}{\sigma_{e,j-1}}\right)^2 + \frac{1}{2}\left(\frac{1}{\sigma_j^2} + \frac{1}{\sigma_{e,j-1}^2}\right)(\mu_{e,j-1} - \mu_j)^2, \tag{3}$$

$$J(D_{i,j-1}D_j) = \frac{1}{2}\left(\frac{\sigma_{i,j-1}}{\sigma_j} - \frac{\sigma_j}{\sigma_{i,j-1}}\right)^2 + \frac{1}{2}\left(\frac{1}{\sigma_j^2} + \frac{1}{\sigma_{i,j-1}^2}\right)(\mu_{i,j-1} - \mu_j)^2. \tag{4}$$

The Jeffreys divergence measure is a symmetric form of the Kullback-Leibler divergence measure. It is a function of the means and standard deviations of the two distributions being compared. Hence, it is an appropriate distance measure for bivariate distributions. We choose the winner distribution $D_{w,j-1}$ ($w = e$ or i) at step j as the one whose Jeffreys distance from the training population D_j is the smallest. The mean and variance of the winning distribution are then updated at each step as follows:

$$\mu_{w,j} = \frac{\mu_{w,j-1} + \mu_j}{2}, \tag{5}$$

$$\sigma_{w,j}^2 = \frac{\sigma_{w,j-1}^2 + \sigma_j^2}{2}. \tag{6}$$

The loser distribution retains its previous values.

We iterate this process for all the training populations except those that were marked as initial clusters. At the end of the process, we obtain the estimates of the two distributions corresponding to the expiration and nonexpiration phases of the breathing cycle. Figure 5 depicts our *K*-means training method.

Testing Phase

During the testing phase, we represent at frame t each pixel x_t in region R as a mixture of two distributions:

$$f(x_t) \sim \pi_{e,t} N\left(\mu_{e,t}, \sigma_{e,t}^2\right) + \pi_{i,t} N\left(\mu_{i,t}, \sigma_{i,t}^2\right), \tag{7}$$

where $f_e(x_t) \sim N(\mu_{e,t}, \sigma_{e,t}^2)$ is the normal expiration distribution, $f_i(x_t) \sim N(\mu_{i,t}, \sigma_{i,t}^2)$ is the normal nonexpiration distribution, and $\pi_{e,t}$ and $\pi_{i,t}$ are their respective weights in the mixture satisfying the criterion

$$\pi_{e,t} + \pi_{i,t} = 1.$$

In the beginning of the testing phase ($t = 0$), the distributions for nonexpiration and expiration are equiprobable with $\pi_{e,t} = \pi_{i,t} = 0.5$ and are parameterized by the respective means and variances that we computed during the training phase. Therefore, every pixel in region R is represented as having the following starting distribution:

$$f(x_0) \sim 0.5\, N\left(\mu_{i,0}, \sigma_{i,0}^2\right) + 0.5\, N\left(\mu_{e,0}, \sigma_{e,0}^2\right). \tag{8}$$

At time $t > 0$ and for pixel x_t, we compare the incoming temperature value from the sensor with the estimated distribution from the previous frame at time t–1. For this comparison to be effective, we consider that the incoming temperature θ_{x_t} can be associated to a normal distribution $g(\theta_{x_t}) \sim N(\mu_{g,t}, \sigma_{g,t}^2)$, where $\mu_{g,t} = \theta_{x,t}$ and $\sigma_{g,t} = NEDT$. For the camera model that we use, $NEDT = 0.01\ ^\circ\text{C}$.

We compute the Jeffreys divergence measures between the incoming distribution $g(\theta_{x_t})$ and the existing nonexpiration $f_i(x_{t-1})$ and expiration $f_e(x_{t-1})$ distributions, respectively. Specifically,

$$J(f_i(x_{t-1}), g(\theta_{x_t})) = \frac{1}{2}\left(\frac{\sigma_{i,t-1}}{\sigma_{g,t}} - \frac{\sigma_{g,t}}{\sigma_{i,t-1}}\right)^2 + \frac{1}{2}\left(\frac{1}{\sigma_{g,t}^2} + \frac{1}{\sigma_{i,t-1}^2}\right)(\mu_{i,t-1} - \mu_{g,t})^2, \tag{9}$$

$$J(f_e(x_{t-1}), g(\theta_{x_t})) = \frac{1}{2}\left(\frac{\sigma_{e,t-1}}{\sigma_{g,t}} - \frac{\sigma_{g,t}}{\sigma_{e,t-1}}\right)^2 + \frac{1}{2}\left(\frac{1}{\sigma_{g,t}^2} + \frac{1}{\sigma_{e,t-1}^2}\right)(\mu_{e,t-1} - \mu_{g,t})^2. \tag{10}$$

We consider that the incoming distribution is closer to the existing distribution that features the minimum Jeffreys divergence measure. We call this the *winning distribution* $f_w(x_{t-1})$ and the other the *losing distribution* $f_l(x_{t-1})$. Based on this information, we update the parameters of the mixture following the method of moments. Specifically, we update the weights for both distributions and the mean and variance of the winning distribution only. The mean and variance of the losing distribution remain the same.

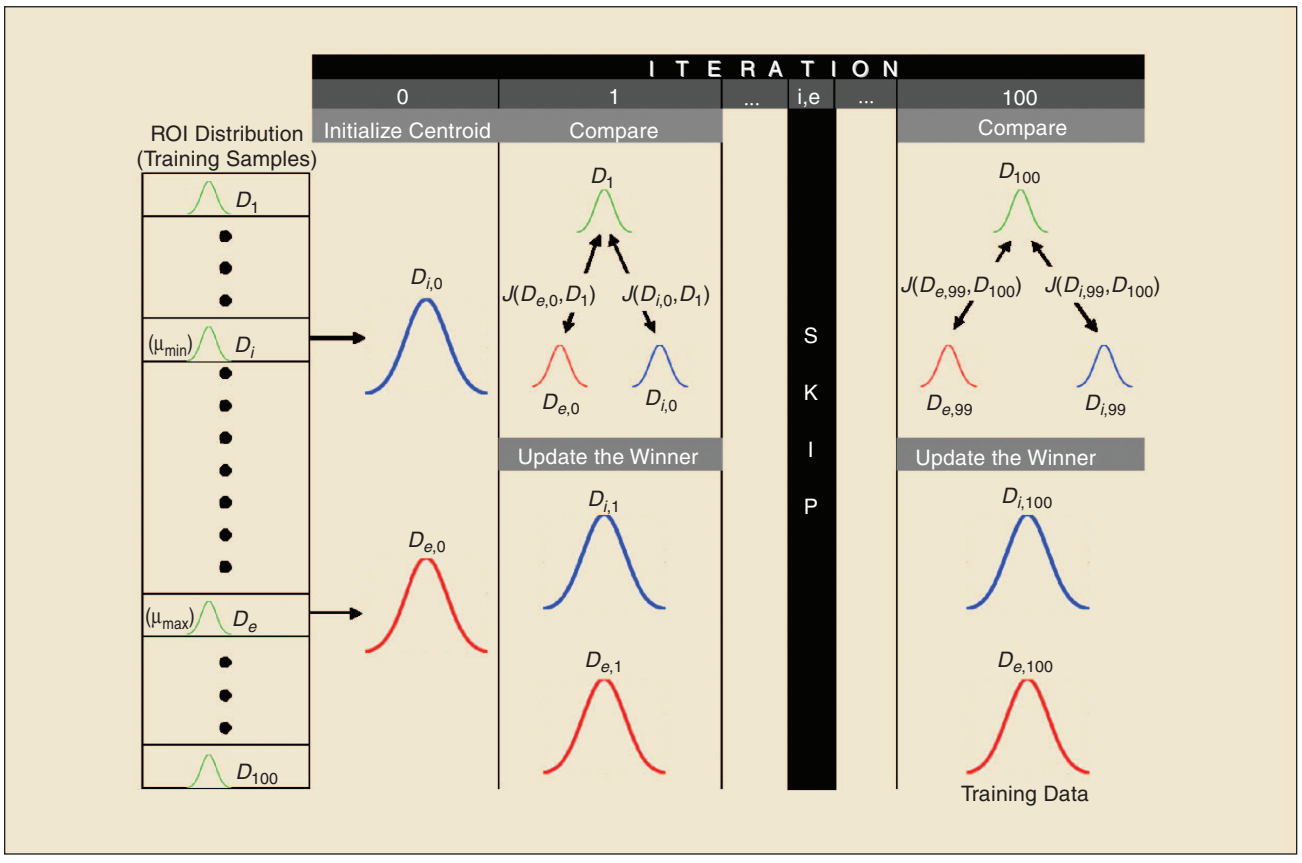

Fig. 5. Iterations in the *K*-means training data acquisition method. The resulting expiration and nonexpiration distributions at the end of the M=100$^{\text{th}}$ iteration are used to jump-start the testing phase.

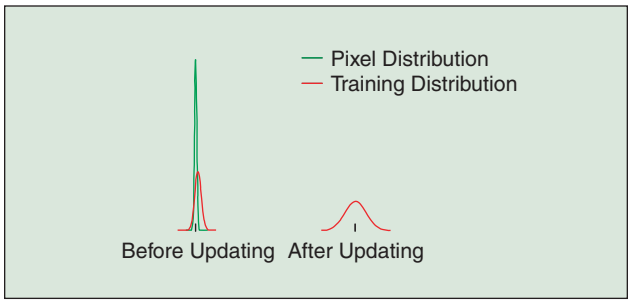

Fig. 6. Comparison of a training distribution before and after the application of the method of moments.

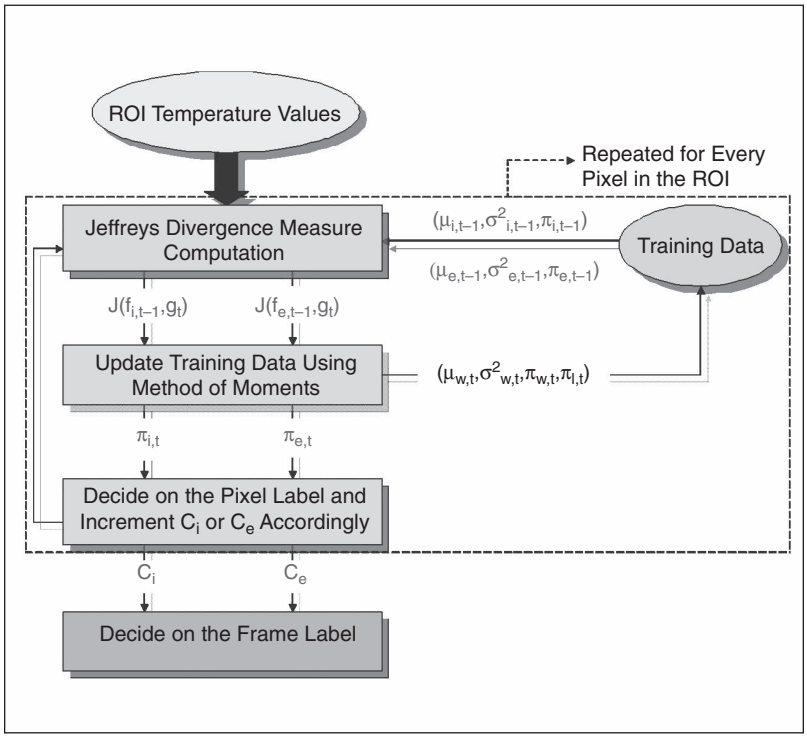

Fig. 7. Overview of the statistical methodology for labeling infrared video frames as expiration or nonexpiration.

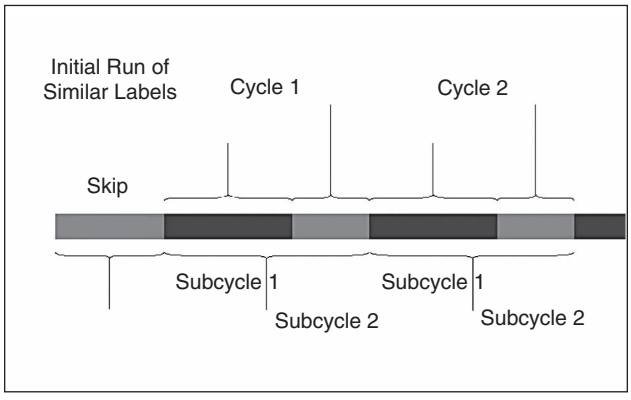

Fig. 8. An example labeling of the video frame line and computation of the breathing rate.

The weights of the winning and losing distributions are updated as follows:

$$\pi_{w,t} = (1-\rho)\pi_{w,t-1} + \rho, \tag{11}$$

$$\pi_{l,t} = (1-\rho)\pi_{l,t-1}. \tag{12}$$

The mean and variance of the winning distribution are updated as follows:

$$\mu_{w,t} = (1-\rho)\mu_{w,t-1} + \rho\mu_{g,t}, \tag{13}$$

$$\sigma^2_{w,t} = (1-\rho)\sigma^2_{w,t-1} + \rho\sigma^2_{g,t} + \rho(1-\rho)(\mu_{g,t} - \mu_{w,t-1})^2. \tag{14}$$

The parameter ρ is a learning parameter that is computed from the following formula [23]:

$$\rho = e^{-\frac{1}{2}\left[\frac{\frac{1}{2}(\mu_{g,t}-\mu_{w,t-1})}{\sigma_{w,t-1}}\right]^2}. \tag{15}$$

Figure 6 is a visualization example of how the incoming distribution may affect the existing distribution. The updated data acts as the new estimate for the corresponding pixel in the next incoming frame.

The pixel x_t is given the label of the distribution with the highest updated weight. A count is kept of the number of expiration C_e and nonexpiration C_i pixels in region R at time t. Once all the pixels in region R are processed, the frame gets the label of the most frequently occurring pixel label. For example, if $C_i > C_e$, the frame is labeled as nonexpiration; otherwise, the frame is labeled as expiration. Figure 7 shows the flow of control and data through the statistical algorithm.

The breathing rate computation algorithm keeps track of the frame labels and continuously updates the time of the current breathing cycle T_c by using the current timestamp T_n and the previous timestamp T_{n-1}. The

Fig. 9. Phoenix midwave infrared camera equipped with a 50-mm lens.

initial run of similar frame labels (Figure 8) is skipped since the testing phase might have started in the middle of a cycle. The algorithm keeps track of the two subcycles in the breathing cycle, and once it detects the beginning of the next cycle, the breathing rate of the current cycle is computed in cycles/min using the formula

$$\text{Rate} = \frac{60}{T_c} \text{ cycles/min.} \quad (16)$$

Experimental Setup

We used a cooled midwave infrared Phoenix camera with a spectral range of $3.0 - 5.0\ \mu$m (Indigo Systems, Goleta, California) equipped with a 50-mm lens (Figure 9). The focal plane array of the camera is $FPA = 640 \times 512$ pixels in size and has thermal sensitivity $NEDT = 0.01\ ^\circ$C. An external black body (Santa Barbara Infrared, Santa Barbara, California) was used to calibrate the camera. Infrared video frames were acquired at a rate of 31 frames/s.

We captured the profile view of the subject's face and respiratory airflow from a distance of 6–8 ft (Figure 10). A piezo-strap transducer [Figure 11(a)] wrapped around the subject's diaphragm measured the thoracic circumference during expiration and nonexpiratory phase. The transducer sent its signal to a PowerLab data acquisition system [ADI Instruments, Australia—Figure 11(b)]. This was the gold standard that we used for benchmarking the infrared imaging measurements.

Experimental Results

In this section, we investigate experimentally different aspects of the breathing function and our method's parameters. We also describe the performance of our noncontact methodology against ground-truth measurements taken by the PowerLab/4SP ADI instrument.

When air is breathed in, it gets warmed up during its passage into the respiratory system and during its brief stay in the lungs. Figure 12 shows the plot of mean ROI temperature along the timeline for one of the subjects in our dataset. From the plot, we observe that the ROI temperature increases by around 0.1 $^\circ$C during expiration. Figure 13 shows the plot of ROI variance along the timeline for one of the subjects in our dataset. From the plot, we observe that the ROI variance during expiration is quadrupled. This is because within the ROI, there are clusters of hot air molecules interspersed with cold

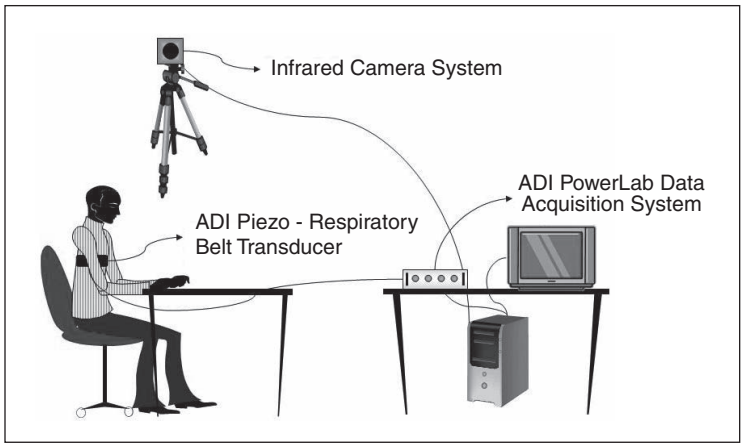

Fig. 10. Experimental setup with the profile view of the subject's face captured by a midwave infrared Phoenix camera and ground-truth data recorded concomitantly using a piezo-strap transducer and a PowerLab data acquisition system.

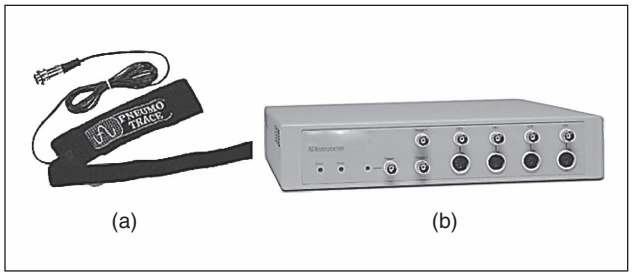

Fig. 11. (a) The piezo-strap transducer and (b) the PowerLab data acquisition system.

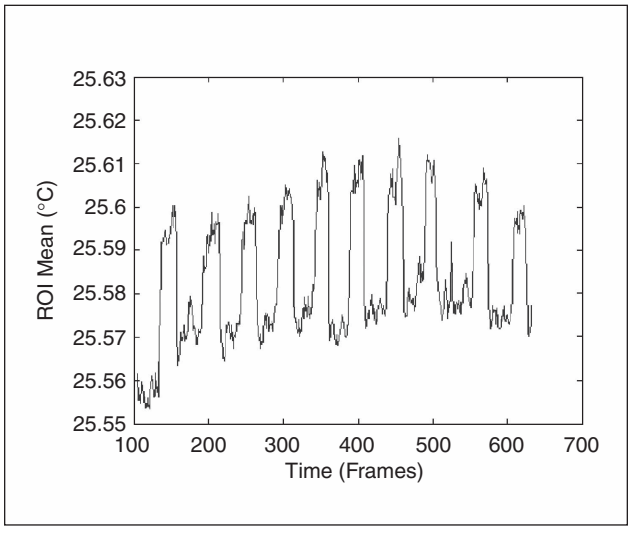

Fig. 12. A plot of the mean pixel temperature in the ROI along the timeline.

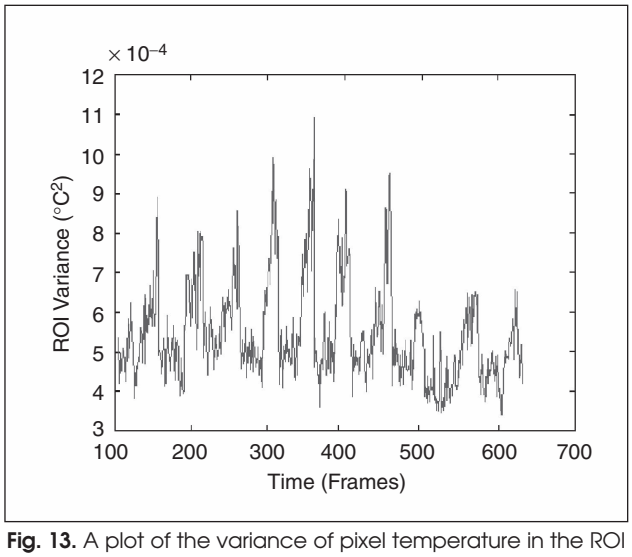

Fig. 13. A plot of the variance of pixel temperature in the ROI along the timeline.

Highly automated, noncontact monitoring of breathing function may have a significant impact on certain biomedical applications.

air resident in the room. The hot air molecules are the ones recently expired through the nostrils.

Our experimental protocol called for measurements during the following phases:

- breathing while the subject rests in a chair
- breathing after the subject has stepped on and off a foot step 30 times in 30 s
- breathing after the subject rested for 10 min so that his physiology reverts back to baseline
- breathing after the subject has stepped on and off a foot step 60 times in 60 s.

We measured the performance of our method on eight thermal clips captured from three subjects. The thermal clips were 1,000 frames long. The first 100 frames of each clip were used for training and the remaining 900 frames for testing. We were able to perform the infrared imaging measurements for all four phases of the experimental protocol only for Subject 2. For the other two subjects, we had to discard some of the measurements because of technical problems in synchronizing the camera with the ADI vital signs monitor.

Since the performance of the method clearly depends on the size of the ROI where the statistical computation is taking place, we have experimented with three different ROI sizes: small (7×3 pixels), medium (21×9 pixels), and large (63×27 pixels). From the experimental results in Table 1, we observe that the medium-size ROI outperforms the other two sizes. The interesting fact is that there is a clear breakdown in performance when the ROI size is getting large. In such a case, a significant number of the ROI pixels are background and not expiratory pixels. As a result, they bias the ROI labeling towards nonexpiration, and the accuracy drops. The absolute ROI sizes are of course dependent on the optics. In our specific experimental scenario, we recorded from a distance of 6–8

Table 1. The accuracy of breathing rate measurements for three different sizes of ROI. The accuracy was determined by ground-truthing the results from our algorithm against concomitant measurements recorded with the ADI vital signs monitor.

Subject	Video Clip	Small ROI	Medium ROI	Large ROI
1	1	98.19	94.32	57.71
	2	92.59	96.14	83.03
	3	97.50	97.74	97.31
2	1	94.76	96.70	67.34
	2	97.91	93.36	78.26
	3	99.23	99.31	56.65
	4	98.06	99.05	97.95
3	1	87.71	94.82	67.62
Average Accuracy (%)		**95.74**	**96.43**	**75.73**

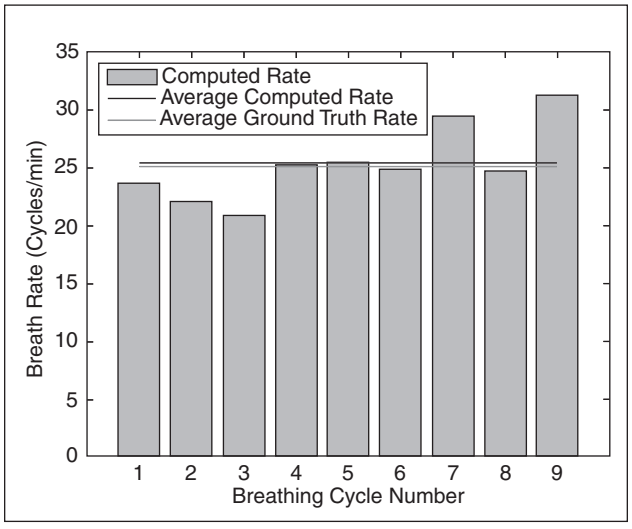

Fig. 14. Breathing rate measurements during the initial resting phase for Subject 2.

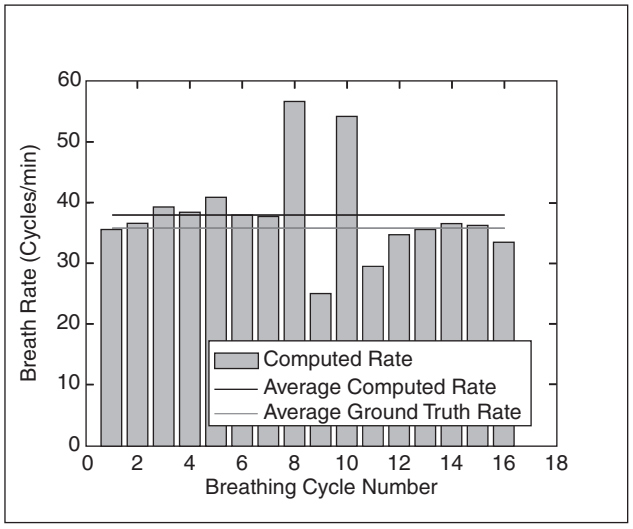

Fig. 15. Breathing rate measurements after 30 s of exercise for Subject 2.

Infrared imaging for measuring breathing function is based on the fact that exhaled air has a higher temperature than the typical background of indoor environments.

ft with a 50-mm lens, and the ROI sizes we cite are commensurate to this optical arrangement.

Figures 14–17 show the variation of breathing rate computed through the infrared imaging method for the four phases of the experimental protocol for Subject 2. They also show the comparison between the mean breathing rate computed through the infrared imaging method and the mean ground-truth rate measured by the ADI vital signs monitor. From the plots, we observe that the breathing rate increases from 12–20 cycles/min during rest to 30–40 cycles/min after the brief exercise. The accuracy of the infrared imaging method appears to be consistent during rest as well as during active periods.

The ground truth signal has output proportional to the expansion (positive-level signal) and relaxation (zero-level signal) of the breathing monitor belt during inspiration and expiration, respectively. The signal computed from the infrared imaging method has output labeled either as nonexpiration or expiration. To make the comparison between ground-truth data and algorithmic results easier, we have digitized both signals by assigning a zero-level signal to nonexpiration and a positive-level signal to expiration. In addition, we have assigned a negative signal level to frames used for acquiring training data. In Figure 18, we can observe that the cycles detected by the infrared imaging method are slightly out of phase with the ground-truth cycles. This accounts for the small discrepancy that exists between the measurements of the infrared imaging method (middle ROI) and the ground-truth instrument.

Three primary factors account for this phase shift:

- imperfect (manual) synchronization of the beginning of the two recordings (infrared video and monitor belt)
- mismatch of recording frequencies (our infrared camera records at 31 frames/s, while the monitor belt samples at 100 times/s)
- the monitor belt records ground-truth data at the diaphragm level, while our infrared imaging method classifies airflow at the nasal-mandible level.

The first factor can be addressed by developing a hardware trigger. The second factor can be addressed by downsampling the ground-truth signal. The amount of phase shift due to the third factor can be determined and taken into account by performing further research in this direction.

Conclusions

Breathing function is one of the major indicators of an individual's health. It can be used to predict various life threatening disorders like sudden infant death syndrome and heart attacks. It is also used in sleep studies to detect sleep apnea. Finally, it is one of the psychophysiological channels in polygraph examinations. Various modalities have been developed to measure breathing rate. Almost all the legacy methods require contact; therefore, they compromise the subject's comfort and mobility. Moreover, measurements by these methods are corrupted either by movement artifacts or by their dependence on other physiological variables, like heart rate. We have proposed a method that is based on infrared imaging and statistical

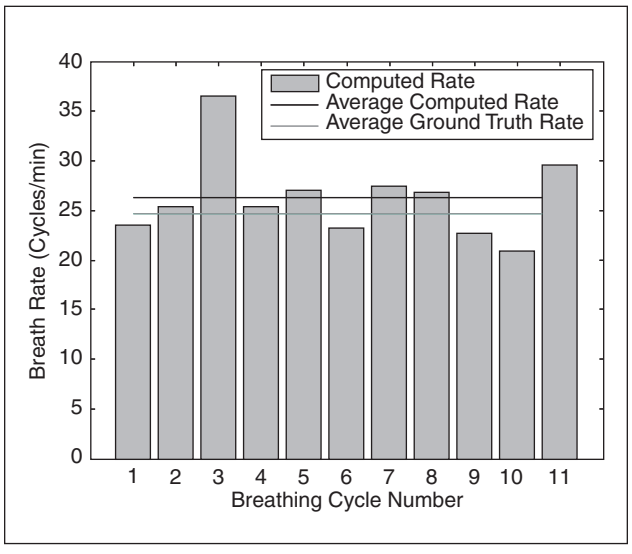

Fig. 16. Breathing rate measurements after 10 min rest for Subject 2.

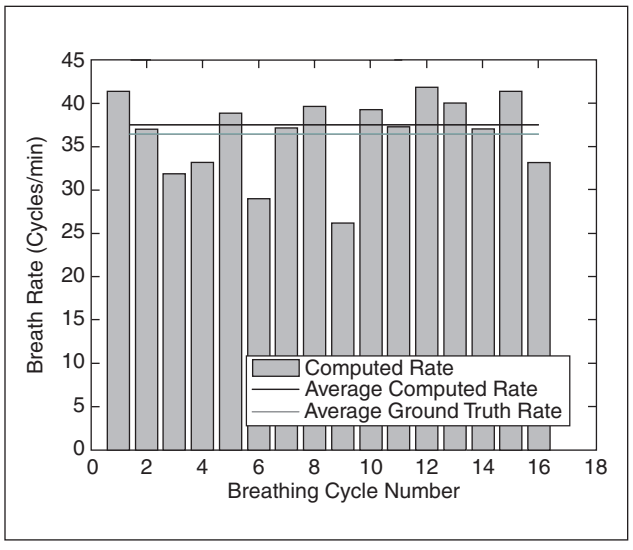

Fig. 17. Breathing rate measurements after 60 s of exercise for Subject 2.

computation to passively measure breathing rate at a distance. This method achieved an accuracy of 96.43% on a small set of subjects during rest and after brief exercise. It has the potential to provide a unique capability for sustained monitoring of chronic or acute breathing problems and in sleep studies by overcoming the deficiencies of the existing measurement modalities. It also opens the way for the next generation contact-free polygraphy that will not affect the subject's psychophysiology.

Future Work

Since our method is contact free, it has significant advantages over contact modalities like ECG, PPG, nasal temperature probe, and breathing monitor belt in terms of comfort. With the use of a simple tracking algorithm, our method has overcome the drawback of active noncontact modalities, like the radar vital signs monitor, whose output gets corrupted by motion artifacts. But, our tracking algorithm cannot deal with situations wherein the ROI fails to remain in the field of respiratory airflow, which occur when the subject rotates his/her head towards or away from the camera (Figure 19) or the source of airflow (either the nose or the mouth) changes.

The first problem may be addressed by developing an advanced nasal-mandible tracking algorithm (Figure 20) along with further research on detecting the respiratory airflow signal in frontal views. The second problem can be addressed by using two ROIs, one each for nasal and mandible airflow (Figure 21).

In our algorithm, we have made use of the Gaussian nature of the thermal signature of breath to develop a statistical algorithm that classifies the frames as expiration or nonexpiration. An alternative approach would be to consider the quasiperiodic nature of the thermal signal (Figures 12 and 13), which renders itself naturally to fast Fourier transforms.

Although our system is meant to be used in climate-controlled environments like modern clinics and homes, an intriguing question is how it will perform in more challenging environmental conditions. In future studies, we will study carefully the effect of rapid temperature changes in the environment on the performance of our method. Theoretically, the adaptive statistical mechanism of the method is expected to cope well in most cases. It would be valuable, however, to establish experimentally the operational envelope of our system.

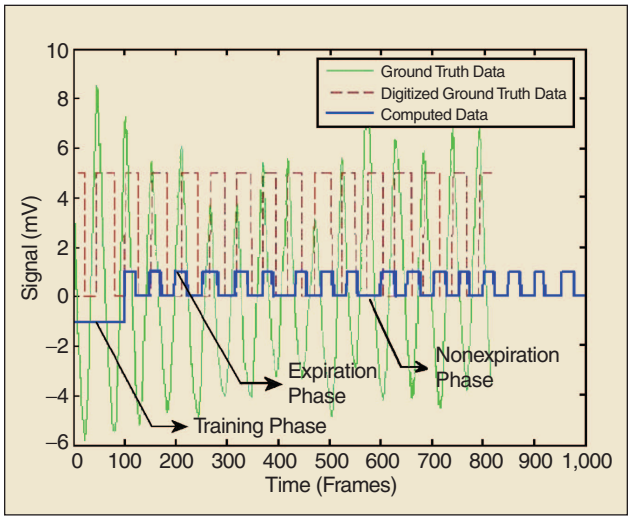

Fig. 18. This plot shows the phase shift between the breathing signal (Subject 2, Clip 4) computed from the infrared imaging method and the correponding ground-truth signal.

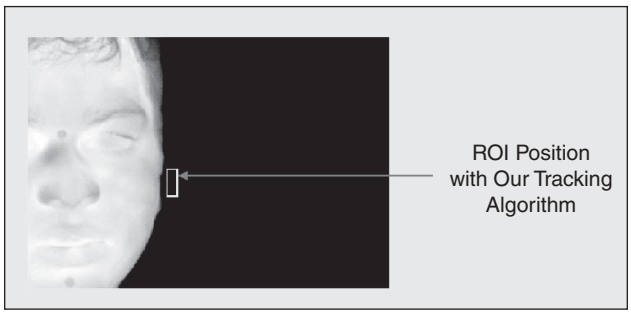

Fig. 19. ROI wrongly positioned when the subject turns his head towards the camera due to the loss of the reference point.

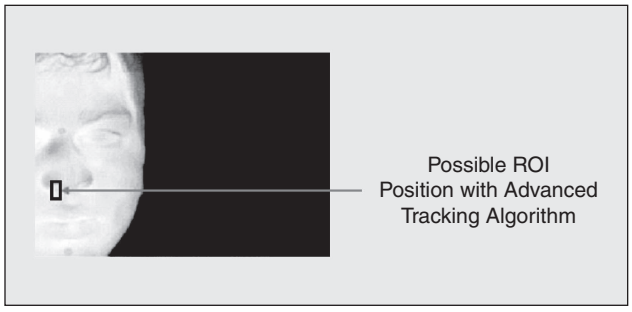

Fig. 20. Likely position of ROI if advanced tracking algorithms were employed.

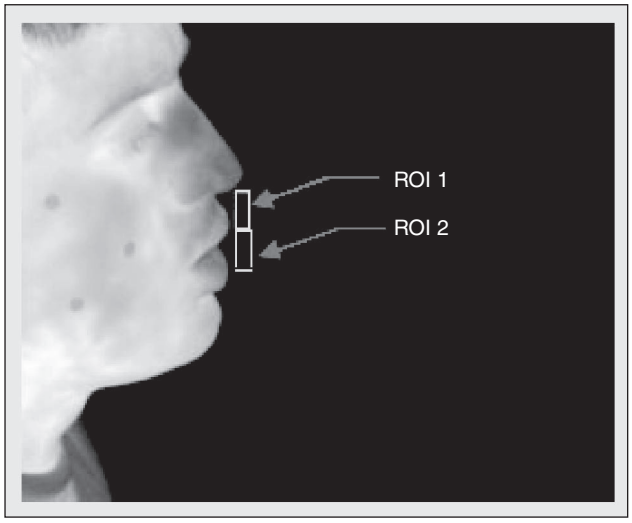

Fig. 21. The problem of a change in source of respiratory airflow can be solved by using an ROI each at the nose and the mouth.

Future studies will be conducted with larger sample sizes and subjects having undergone various degrees of physical exertion. Such studies will establish how well the method scales up to the general population. Although, the answer to this question is pending, the current work clearly establishes for the first time the feasibility of monitoring breathing function in a contact-free manner and with totally passive means.

Acknowledgments

This research was supported by the National Science Foundation (grant IIS-0414754), by DARPA (NSF grant N00014-03-1-0622), and by the University of Houston start-up funds of Prof. I. Pavlidis. The views expressed in this article do not necessarily reflect the views of the funding agencies. We are thankful to Dr. Ephrain Glinert at NSF and Dr. Ralph Chatham at DARPA for their support. We would also like to thank Dr. Arcangelo Merla for his valuable help in the human experiments and Dr. Panagiotis Tsiamyrtzis for many valuable discussions on advanced statistics issues.

Ramya Murthy received an M.S. degree in computer science from the University of Houston and a B.E. degree in computer science and engineering from Bangalore University, India. She worked in the field of infrared imaging as a research assistant in the Computational Physiology Lab at the University of Houston, Texas. Before pursuing her M.S. degree, she worked as a software engineer at Robert Bosch India Limited in the field of embedded mobile communications. She is a scientific programmer in the Laboratories for Biocomputing and Imaging at the University of Texas Medical School in Houston, where she performs algorithmic research and develops software tools for two- and three-dimensional modeling and visualization of biomolecular structures.

Ioannis Pavlidis holds M.S. and Ph.D. degrees in computer science from the University of Minnesota, an M.S. degree in robotics from the Imperial College of the University of London, and a B.S. degree in electrical engineering from Democritus University in Greece. He joined the Computer Science Department at the University of Houston, Texas, in September 2002. His current research interests are in computational medicine, where he is charting new territory. He has developed a series of methods to compute vital signs of subjects in an automated, contact-free, and passive manner. This new technology has found widespread applications in computational psychology and is expected to find additional applications in preventive medicine. The quantification of stress in particular, through the computation of periorbital blood perfusion, is his most well-known piece of research. It is this research that established him as one of the founders of modern lie detection technology. He is a Fulbright Fellow, a Senior Member of the IEEE, and a member of the ACM. He also serves as associate editor for the journal *Pattern Analysis and Applications* (Springer), and he has chaired numerous major IEEE conferences.

Address for Correspondence: Ramya Murthy, 3030 Hidden Mist Court, Pearland, TX 77584 USA. Phone: +1 713 436 9157. E-mail: Ramya.Murthy@mail.uh.edu.

References

[1] G.B. Moody, R.G. Mark, M.A. Bump, J.S. Weinstein, A.D. Berman, J.E. Mietus, and A.L. Goldberger, "Clinical validation of the ECG-derived respiration (EDR) technique," *Comput. Cardiol.*, vol. 13, pp. 507–510, 1986.

[2] T. Kim and M.C.K. Khoo, "Estimation of cardio respiratory transfer under spontaneous breathing conditions: A theoretical study," *Amer. J. Physiol.*, vol. 273, no. 2, pp. H1012–H1023, Aug. 1997.

[3] M. Partinen, J. Alihanka, and J. Hasan, "Detection of sleep apneas by the static charge-sensitive bed," in *Proc. 6th European Congress Sleep Research*, Zurich, Mar. 1982, pp. 312.

[4] B.H. Larson, "Signal processing techniques for non-invasive monitoring of respiration and heart rate," M.S. thesis, Dept. Electrical Sci., Univ. Houston, May 1987.

[5] D. Barschdorff and W. Zhang, "Respiratory rhythm detection with plethysmographic methods," in *Proc 16th Annual Int. Conf. IEEE/EMBS,* Baltimore, MD, Nov. 1994, pp. 912–913,.

[6] L.M. Vicente, A.B. Barreto, and A.M. Taberner, "DSP removal of respiratory trend in photoplethysmographic blood volume pulse measurements," in *Proc. IEEE Southeastcon '96–Bringing Together Education, Sci, and Technol.*, pp. 96–98, 98a,

[7] A. Johansson, L. Nilsson, S. Kalman, and P.A. Oberg, "Respiratory monitoring using photoplethysmography—Evaluation in the postoperative care unit," in *Proc. 20th Annu. Int. Conf. IEEE Eng. Med. Biol. Soc.*, 1998, vol. 20, no. 6, pp. 3226.

[8] K. Nepal, E. Biegeleisen, and T. Ning, "Apnea detection and respiration rate estimation through parametric modeling," in *Proc. 28th IEEE Annu. Northeast Bioengineering Conf.*, Philadelphia, PA, 20–21 Apr. 2002, pp. 277–278.

[9] K. Storck, M. Karlsson, P. Ask, and D. Loyd, "Heat transfer evaluation of the nasal thermistor technique," *IEEE Trans. Biomed. Eng.*, vol. 43, no. 12, pp. 1187–1191, Dec. 1996.

[10] E.F. Greneker, "Radar sensing of heartbeat and respiration at a distance with applications of the technology," *RADAR*, vol. 97, no. 449, pp. 150–154, Oct. 1997.

[11] E.F. Greneker and J.L. Geisheimer, "The RADAR flashlight three years later: An update on developmental progress," in *Proc. IEEE 34th Annu. Int. Carnahan Conf. Security Technol.*, 2000, pp. 170–173

[12] J. Geisheimer and E.F. Greneker III, "A non-contact lie detector using radar vital signs monitor (RVSM) technology," in *Proc. IEEE 34th Annu. 2000 Int. Carnahan Conf. Security Technology*, pp. 257–259.

[13] I. Pavlidis, J. Levine, and P. Baukol, "Thermal imaging for anxiety detection," in *Proc. 2000 IEEE Workshop Computer Vision Beyond Visible Spectrum: Methods and Applications*, Hilton Head Island, SC, pp. 104–109.

[14] I. Pavlidis, N.L. Eberhardt, and J. Levine, "Human behavior: Seeing through the face of deception," *Nature*, vol. 415, no. 6867, Jan. 3, 2002.

[15] I. Pavlidis and J. Levine, "Thermal image analysis for polygraph testing," *IEEE Eng. Med. Biol. Mag.*, vol. 21, no. 6, pp. 56–64, Nov./Dec. 2002.

[16] D.U. Silverthorn, "Respiratory physiology," in *Human Physiology: An Integrated Approach*, 2nd ed. Englewood Cliffs, NJ: Prentice-Hall, 2001, pp. 498–508.

[17] R. Murthy, "Feasibility study of breathing rate computation using infrared imaging, M.S. thesis," Dept. Comput. Sci., Univ. Houston, Dec. 2004.

[18] N. Otsu, "A threshold selection method from gray-level histograms," *IEEE Trans. Syst., Man, Cybern.*, vol. 9, no. 1, pp. 62–65, 1979.

[19] G.C. Holst, *Common Sense Approach to Thermal Imaging*. Bellingham, WA: SPIE, 2000, p. 144.

[20] M. Sonka, V. Hlavac, and R. Boyle, *Image Processing, Analysis, and Machine Vision*, 2nd ed. Pacific Grove, CA: Brooks/Cole, 2001.

[21] I. Pavlidis, V. Morellas, P. Tsiamyrtzis, and S. Harp, "Urban surveillance systems: From the laboratory to the commercial world," *Proc. IEEE*, vol. 89, no. 10, pp. 1478–1497, Oct. 2001.

[22] J.T. Tou and R.C. Gonzalez, *Pattern Recognition Principles*. Reading, MA: Addison-Wesley, 1974.

[23] A. Pednekar, I.A. Kakadiaris, and U. Kurkure, "Adaptive fuzzy connectedness-based medical image segmentation," in *Proc. 2002 Indian Conf. Computer Vision, Graphics, Image Processing* (ICVGIP'02), Ahmedabad, India, pp. 457–462.